Journal of Solid State Chemistry 187 (2012) 103–108

Contents lists available at SciVerse ScienceDirect

Journal of Solid State Chemistry

journal homepage: www.elsevier.com/locate/jssc

Effects of oxygen vacancy and N-doping on the electronic and photocatalytic properties of Bi_2MO_6 (M=Mo, W)

Kangrong Lai [a,b], Wei Wei [a], Yingtao Zhu [a], Meng Guo [a], Ying Dai [a,*], Baibiao Huang [a]

[a] School of Physics, State Key Laboratory of Crystal Materials, Shandong University, Shanda South Road 27#, Jinan 250100, PR China
[b] Departments of Physics, Changji University, Changji 831100, PR China

ARTICLE INFO

Article history:
Received 1 November 2011
Received in revised form
28 December 2011
Accepted 2 January 2012
Available online 10 January 2012

Keywords:
Bi_2MO_6
Photocatalytic
Defect
Mechanism

ABSTRACT

The electronic properties of Bi_2MO_6 (M=Mo and W) are studied by using the first-principles calculations. It is attributed to its smaller electron effective mass that Bi_2WO_6 has higher photocatalytic activity than Bi_2MoO_6. The oxygen vacancy in Bi_2MO_6 serves as a trapping center of photogenerated electrons and thus is in favor of the photocatalytic efficiency. Nitrogen-doping induces localized structure distortion and thus improves the separation of photogenerated electron-hole pairs. Moreover, band gaps decrease obviously with doping concentration increasing, therefore the photoabsorption edges will give rise to a redshift in Bi_2MO_6.

1. Introduction

Concerning the environmental pollution and energy shortage, semiconductor photocatalysts have been paid much attention due to the applications in solar energy conversion and photo-oxidation of organic pollutants [1–3]. In the past years, TiO_2 as a photocatalyst has been investigated extensively because of its high reactivity, low cost and environmentally friendly features [4,5]. Nevertheless, due to its wide band gap of about 3.0 eV, TiO_2 can only absorb ultraviolet (UV) light, which is less than 5% in the whole energy of the incoming solar light. Hence, effective utilization of solar energy becomes the main objective in photochemical research nowadays. For the sake of this, many efforts have been dedicated to modify the energy band structure of TiO_2 to shift its spectral response into the visible light region and improve its photocatalytic performance by doping elements, depositing metals on photocatalyst surfaces [6,7]. On the other hand, exploring new types of photocatalysts except TiO_2 has also become a crucial subject for higher energy conversion efficiency. Many efforts have been made to exploit active oxide photocatalysts for visible sunlight harvesting. Some binary, ternary and multicomponent metal oxide photocatalysts with intense visible light absorption and high activity, such as $SrTiO_3$ [8], $CaIn_2O_4$ [9], Ta_2O_5 [10], $BaTi_4O_9$ [11], ZrO_2 [12], $ReVO_3$ (Re=Ce, Pr, Nd) [13], bismuth oxides [14–18], have been reported. Particularly, Bi-based photocatalysts have attracted much attention because of the up-shifted valence band (VB) and a smaller band gap resulted from hybridization between Bi 6s and O 2p states. At the same time, the hybridization makes the VB more dispersive, which is benefit to the transition of photogenerated holes in the valence band. It has been identified that Bi_2MO_6 (M=W and Mo), with an Aurivillius layered structure composing of MO_6 octahedron and Bi–O–Bi layers, shows promising photocatalytic activity [19–28]. The MO_6 octahedra are connected to each other corner-sharingly. The $(Bi_2O_2)^{2+}$ layers are sandwiched between MO_6 octahedral layers. It is found that the corner-sharing structure makes photogenerated electron-hole pairs migrate easily and transfer effectively to the surface, which contributes to the photocatalytic performance under visible-light [16]. The band gaps of Bi_2MoO_6 have been evaluated to be 2.63 eV [26], 2.58 eV [27] and 2.56 eV (calcined) or 2.59 (uncalcined) [28], while for Bi_2WO_6 are 2.77 eV [26], 2.79 eV [27] and 2.7 eV [23] in different experimental observations. The unique physical and chemical properties, such as chemical inertness, photo stability and environmental friendly features, make them ideal potential photocatalytic materials under visible-light irradiation. However, most of Bi_2MO_6 samples were in general prepared by solid-state reaction, and the photocatalytic activity was low due to the large crystal size and small surface area [21,26]. The photocatalytic activity of semiconductors relates to the separation and migration of photogenerated carriers. Therefore, it is significant and meaningful to promote the separation efficiency and increase the redox power of photogenerated carriers in order to improve the photocatalytic activity of Bi_2MO_6 for practical application. Fu et al. reported that

* Corresponding author. Fax: +86 531 88365569.
E-mail address: daiy60@sina.com (Y. Dai).

0022-4596/$ - see front matter © 2012 Elsevier Inc. All rights reserved.
doi:10.1016/j.jssc.2012.01.004

fluorinated Bi_2WO_6 presents enhanced photoactivity in the degradation process of RhB [29]. Shi and co-workers indicated that fluorinated Bi_2WO_6 shows excellent photoactivity in the degradation process of MB [30]. Shang and Zhang et al. [31,32] demonstrated that nitrogen doped Bi_2WO_6 displays preferable photoactivity in the degradation process of RhB and CH_3CHO under the visible light. The oxygen vacancy (V_o) can be inevitably introduced during the sample preparing process. Zhou [26] and Belver [27] pointed that Bi_2WO_6 exhibites higher photocatalytic activity than Bi_2MoO_6. As a consequence, there are still many issues open for these materials. For example, what is the microscopic origin of the difference in photocatalytic activity between Bi_2WO_6 and Bi_2MoO_6? What are the effects of inevitably existent V_o on the photocatalytic performance? How do N dopants modify the electronic structure and the related photocatalytic properties of Bi_2MO_6? To understand these issues, it is necessary to carry out a more profound and detailed investigation on the electronic structure and related properties of Bi_2MO_6. In the present work, the geometric and electronic structures of Bi_2MO_6 with and without V_o and the effects of N-doping have been examined by means of density functional theory (DFT). Our results may provide new insights and understanding on the photocatalytic mechanisms of Bi_2MO_6 and the influence of V_o and N dopants on the photocatalytic activity.

2. Computational details and models

The first-principles calculations were performed using Vienna ab initio Simulation Package (VASP) [33,34] with the projector augmented wave (PAW) [35] pseudopotential method. Generalized gradient approximation (GGA) [36] in the scheme of the Perdew–Burke–Ernzerhof (PBE) functional [37] was employed to treat the exchange-correlation potentials referring to the previous researches [14–15,30]. We have tested the total energy convergence of 36-atom primitive cell with respect to different plane-wave energy cutoff. The total energies with energy cutoff 300, 350, 400, and 450 eV are −266.334, −263.956, −263.317 and −262.963 eV, respectively. For the sake of more accurate results we used a kinetic energy cutoff of 400 eV. The Brillouin-zone sampling was integrated using Monkhorst–Pack generated sets of k-points [38]. k-points mesh $2\times2\times5$ found to be sufficient to reach convergence for bulk supercell calculations. The outright box geometry optimizations were adopted whose Pulay stress was zero. The convergence threshold for self-consistence-field iteration was set at 10^{-4} eV. Both the atomic positions and cell parameters were optimized until all the residual force components were smaller than 0.02 eV/Å. Band structures were calculated along the paths connecting the following high-symmetry points: Γ (0, 0, 0), F (0, 0.5, 0), Q (0, 0.5, 0.5), and Z (0, 0, 0.5) in the k-space. For both the two structures, the experimental atomic positions were employed as the starting points of relaxation, and subsequent calculations were conducted using the relaxed atomic positions.

The DFT+U method is applied to strong correlation systems and the hybrid density functional methods usually used to improve its band gap values close to experiments [3,39]. GGA method introduces the underestimated band gap because the Kohn–Sham potentials lack pronounced atomic shell structures of accurate potential, which are too shallow in the molecular region and decay faster than Coulombic asymptotic behavior. However, the character of band structure and the trend of the energy gap variations are expected to be reasonable and reliable [14–15,30]. So that, in the present work, the GGA method is employed.

We studied Bi_2WO_6 and Bi_2MoO_6 belonging to the orthorhombic crystal system with space group of Pca2(1). A 72-atom $2\times1\times1$ supercell of relaxed Bi_2WO_6 ($Bi_{16}W_8O_{48}$) employed in the calculations is illustrated in Fig. 1 as a representation. The later discussion will also implement the site notations here. The lattice parameters are $a=5.4326$, $b=16.4302$ and $c=5.4584$ with a cell volume ca. to 487.21 for Bi_2WO_6 [40] and $a=5.4822$, $b=16.1986$ and $c=5.5091$ with a cell volume equal to 489.23 for Bi_2MoO_6 [41].

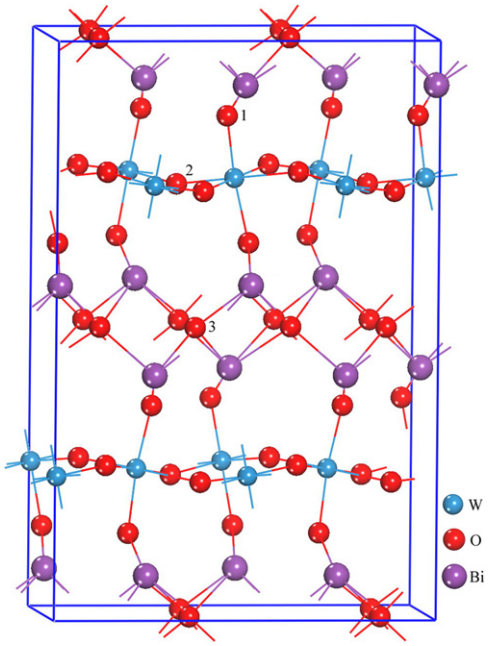

Fig. 1. The 72-atom supercell of Bi_2WO_6. The big purple, the small blue, and the red spheres represent Bi, W and O atoms, respectively. 1, 2 and 3 represent defect position considered in the calculation. (For interpretation of the references to color in this figure legend, the reader is referred to the web version of this article.)

There are three kinds of unequal O sites in this 72-atom supercell: 1, 2 and 3 (see Fig. 1). To understand the effects of V_o on electronic properties of Bi_2MO_6, one V_o was introduced into the supercell of $Bi_{16}M_8O_{48}$ by removing one O atom from one of three unequal sites (see Fig. 1). One and two O atoms (at site 1, 2 and 3 in Fig. 1) were replaced by one and two N atoms in the supercell are employed to simulate the N-doped system with the atomic ration of N to Bi of 0.0625 and 0.125, respectively. This is reasonable and credible to understand the experiments results corresponding to the atomic ration of N to Bi, $R_N=0$, 0.05, 0.25, 0.5, and 0.75 [31]. In the present work, eight different configurations with two N atoms at different O sites were considered. The geometry optimizations were carried out in all of the calculations.

3. Results and discussion

3.1. Defect formation energy

The defect formation energies are firstly examined as following relations to study the relative stability of all relaxed structures.

$$E_{form1}=E(Bi_{16}M_8O_{47})-[E(Bi_{16}M_8O_{48})-\mu_O]$$

$$E_{form2}=E(Bi_{16}M_8NO_{47})-[E(Bi_{16}M_8O_{48})-\mu_O+\mu_N]$$

$$E_{form3}=E(Bi_{16}M_8N_2O_{46})-[E(Bi_{16}M_8O_{48})-2\mu_O+2\mu_N]$$

where E_{form1}, E_{form2} and E_{form3} are the defect formation energies of $Bi_{16}M_8O_{47}$, $Bi_{16}M_8NO_{47}$ and $Bi_{16}M_8N_2O_{46}$, respectively. $E(Bi_{16}M_8O_{47})$, $E(Bi_{16}M_8NO_{47})$, $E(Bi_{16}M_8N_2O_{46})$ and $E(Bi_{16}M_8O_{48})$ denote the total energies of $Bi_{16}M_8O_{47}$, $Bi_{16}M_8NO_{47}$, $Bi_{16}M_8N_2O_{46}$ and $Bi_{16}M_8O_{48}$ supercells, respectively. The values of chemical potentials of nitrogen and oxygen are μ_N and μ_O, which are

determined by the energy of an O or a N atom in an O_2 or a N_2 molecule, $\mu_O = 1/2\mu(O_2)$, $\mu_N = 1/2\mu(N_2)$.

In the case of $Bi_{16}M_8O_{47}$ with one V_o, the calculated defect formation energies of three configurations with V_o at different sites (see Fig. 1) are listed in Table 1. It shows that the V_o in $Bi_{16}M_8O_{47}$ preferably locates at site 2 in MO_6 octahedron adjacent to M in MO_6 octahedron, which is consistent with the result of Islam et al. [42].

For the N-doped Bi_2MO_6 ($Bi_{16}M_8NO_{47}$), the calculated defect formation energies listed in Table 1 indicate that the substitutional N prefers to locate at site 2 adjacent to M in MO_6 octahedron. While for the two N atoms doped cases, eight distinct configurations denoted by 11, 12, 13, 22^a, 22^b, 23, 33^a and 33^b (see Fig. 1, the numbers indicate different O sites, while a and b mean adjacent and opposite sites) are considered. The calculated defect formation energies of these configurations are listed in Table 2. It is demonstrated that the two substitutional N atoms in Bi_2MoO_6 prefer to locate at two neighbor sites next to Mo in MoO_6 octahedron (site 33^b), while in Bi_2WO_6 they prefer to situate at the nearest opposite sites to Bi in the $[Bi_2O_2]^{2+}$ layers (site 22^a).

The corresponding local structures before and after relaxations are displayed in Fig. 2(a)–(e) and Fig. 2 (f)–(j), respectively. It is found that changes in the morphology and symmetry of eight configurations before and after optimization are negligible, which is in consistent with the experimental results of N-doped Bi_2WO_6 [31]. However, the bond lengths near defects are obviously changed, which indicates that defects induce localized structure distortion and cause dipole moment in the crystals. The dipole moment arouses the internal field, which promotes the separation of the photoinduced electrons and holes [43–48]. Meanwhile, lattice strain growing out of distortion deviates the surface oxygen atoms from the lattice, which primarily acts as an efficient e^- trap, leading to the generation of O_2^- and preventing the recombination of photogenerated electrons and holes. A synergistic effect between the two aspects mentioned above can reduce the recombination probability of the photogenerated electrons and holes, and improve the photocatalytic efficiency [49–51].

3.2. Electronic structures

The calculated band structures of pure, V_o-contained and N-doped Bi_2WO_6 and Bi_2MoO_6 are displayed in Fig. 3. The total density of states (TDOS) and projected density of states (PDOS) of pure Bi_2MO_6 are shown in Fig. 4. The TDOS and PDOS of Bi_2WO_6 including one V_o and one or two N atoms are presented in Fig. 5.

Table 1
Defect formation energies of $BiMO_6$ with one O vacancy and one N atom doped.

	Defect formation energy (eV)			
		1	2	3
Bi_2WO_6	O vacancy	3.582	3.576	4.059
	N-doping	5.568	5.205	5.479
Bi_2MoO_6	O vacancy	3.974	2.973	2.979
	N-doping	5.370	5.026	5.411

Table 2
Defect formation energies of $BiMO_6$ with two N atoms doped.

	Defect formation energy (eV)							
	11	12	13	22^a	22^b	23	33^a	33^b
Bi_2WO_6	11.00	10.50	10.47	10.46	10.49	10.50	10.64	10.33
Bi_2MoO_6	10.72	10.08	10.60	10.00	10.10	10.31	10.01	10.28

[a] Adjacent.
[b] Opposite.

3.2.1. Pure Bi_2MO_6

The band structure of $Bi_{16}W_8O_{48}$ shows that the calculated direct band gap is about 1.91 eV (see Fig. 3(a)), which is underestimated compared with the experimental value of 2.79 eV. [27] The difference in the theoretical and experimental band gaps is 0.88 eV. The TDOS and PDOS are shown in Fig. 4(a) displaying that the VB is mainly composed of O 2p, Bi 6s, Bi 6p and small W 5d states, while the CB is formed dominantly by W 5d, Bi 6p and small O 2p states. It is revealed that the visible-light response for Bi_2WO_6 is due to the transition from the hybridized Bi 6s and O 2p states in VB to W 5d states in the CB. Moreover, we can see from Fig. 3 that Bi 6s states mainly contribute to the upper of valence band, the hybridization of Bi 6s and O 2p states makes the VB largely dispersed, which favors the mobility of photoexcited holes in the valence band and thus facilitates the high photocatalytic efficiency [30,52–55].

Bi_2MoO_6 also presents photocatalytic activity under visible light [16,21]. Here, we study orthorhombic Bi_2MoO_6 with space group of Pca2(1). The sample has a corner-sharing structure of MoO_6 octahedron correlated to energy gap and the width of CB, which drives the visible light response and controls the photocatalytic performance. The calculated band structure of $Bi_{16}Mo_8O_{48}$ is similar to that of $Bi_{16}W_8O_{48}$ with the band gap is 1.77 eV (see Fig. 3(b)). This is also underestimated compared with the experimental value of 2.58 eV [27]. The difference between the theoretical and the experimental band gap is 0.81 eV. On the other side, it has been estimated that the VB of Bi_2MoO_6 is composed mainly of O 2p states and the CB derives primarily from Mo 4d states and secondarily from Bi 6p states [16,56]. It is worth mentioning that the difference in the photocatalytic efficiency was dominantly ascribed to the different components in the VB of Bi_2WO_6 and Bi_2MoO_6 [21,26]. Our calculated results (see Fig. 4(b)) indicate that the VB of Aurivillius Bi_2MoO_6 structure is contributed by not only O 2p states, but also Mo 4d, Bi 6s states located at VB edge and small Bi 6p states, while the CB is derived from the Mo 4d, Bi 6p and O 2p states. As a result, different components of VB cannot be responsible for the difference in the photocatalytic efficiency of the two samples. In addition, Belver et al. [26,27] reported that Bi_2WO_6 exhibited higher photocatalytic activity than that of Bi_2MoO_6 under UV–vis light, which could be ascribed not only to the different electronic structures but also to the textural properties and the lower surface area of the Bi_2MoO_6.

It is known that the electronic effective mass is inversely proportional to the curvature of conduction bands [57–58]. Namely, steep band curve means a small effective mass and shallow band curve means a heavy effective mass. The smaller effective mass implies better electron mobility. Comparing the CB bottoms of Bi_2WO_6 and Bi_2MoO_6, from Fig. 3(a) and Fig. 3(b), the CB bottom of Bi_2WO_6 has bigger curvature than Bi_2MoO_6' and therefore smaller effective mass. The smaller effective mass of electrons for Bi_2WO_6 benefits to the separation and migration of photogenerated carriers and thus results in better photocatalytic performance than Bi_2MoO_6. Different electronic effective mass should be one of the important factors leading to the different photocatalytic efficiency between Bi_2WO_6 and Bi_2MoO_6.

3.2.2. Bi_2MO_6 with V_O

To explore the influence of V_o on the electronic properties, the electronic band structures of Bi_2MO_6 with one V_o are examined. The calculated band gap of $Bi_{16}W_8O_{47}$ (Fig. 3(c)) and $Bi_{16}Mo_8O_{47}$ are about 1.44 and 1.34 eV, respectively. The oxygen vacancies could

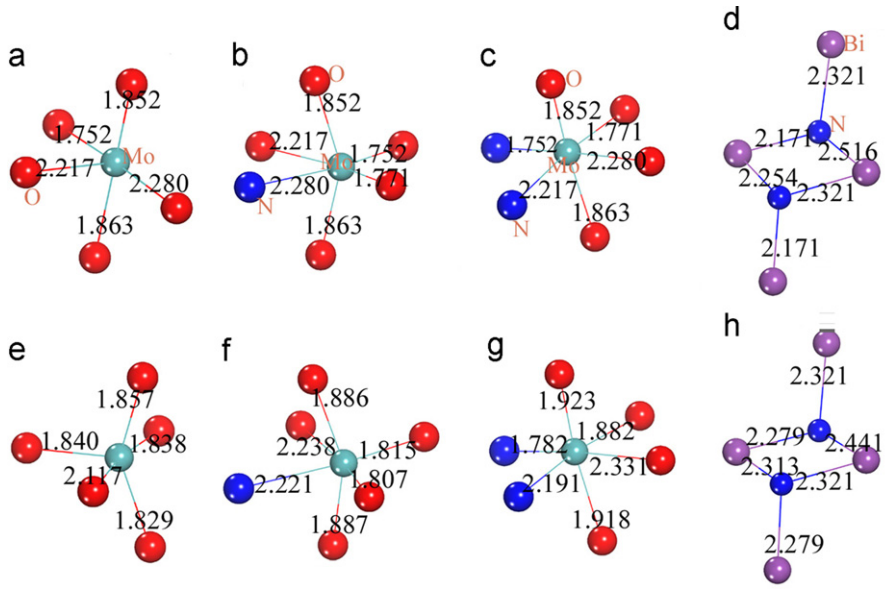

Fig. 2. Defects neighboring structures of (a) before optimizing one O vacancy in Bi_2MoO_6, (b) before optimizing one N atom in Bi_2MoO_6, (c) before optimizing two N atoms in Bi_2MoO_6, (d) before optimizing two N atoms in Bi_2WO_6, respectively. The corresponding optimized structures are shown in (e)–(h), respectively. The unit in bond length is Å.

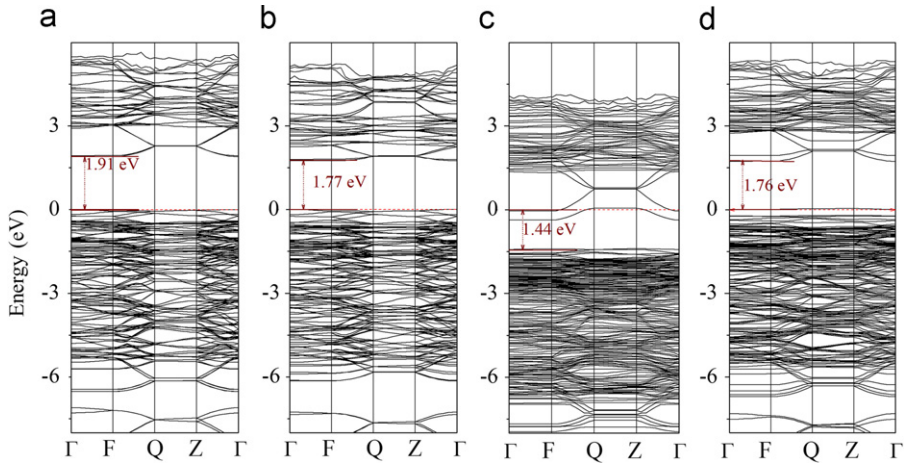

Fig. 3. Band structures of: (a) pure Bi_2WO_6, (b) pure Bi_2MoO_6 (c) Bi_2WO_6 with one O vacancy, (d) Bi_2WO_6 with one N atom. The red dashed line represents the Fermi level. (For interpretation of the references to color in this figure legend, the reader is referred to the web version of this article.)

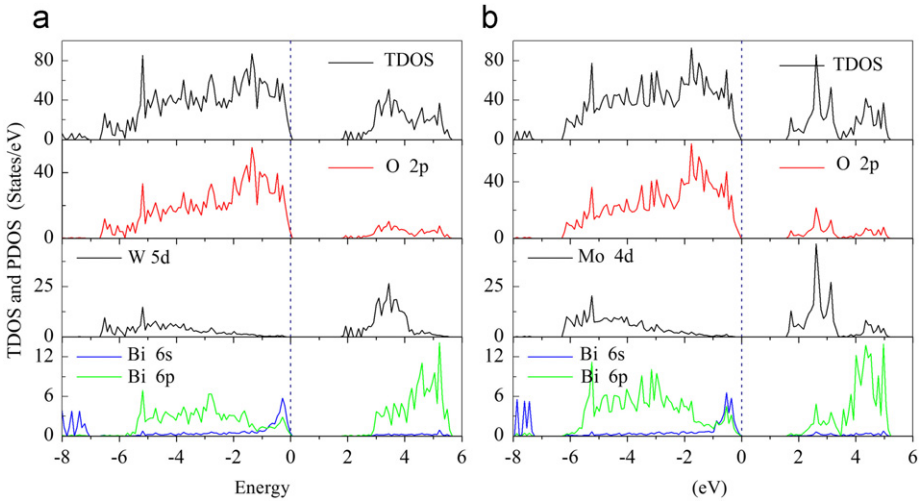

Fig. 4. The total and partial DOS of relaxed Bi_2MO_6: (a) Bi_2WO_6, (b) Bi_2MoO_6. The navy dashed line represents the Fermi level. (For interpretation of the references to color in this figure legend, the reader is referred to the web version of this article.)

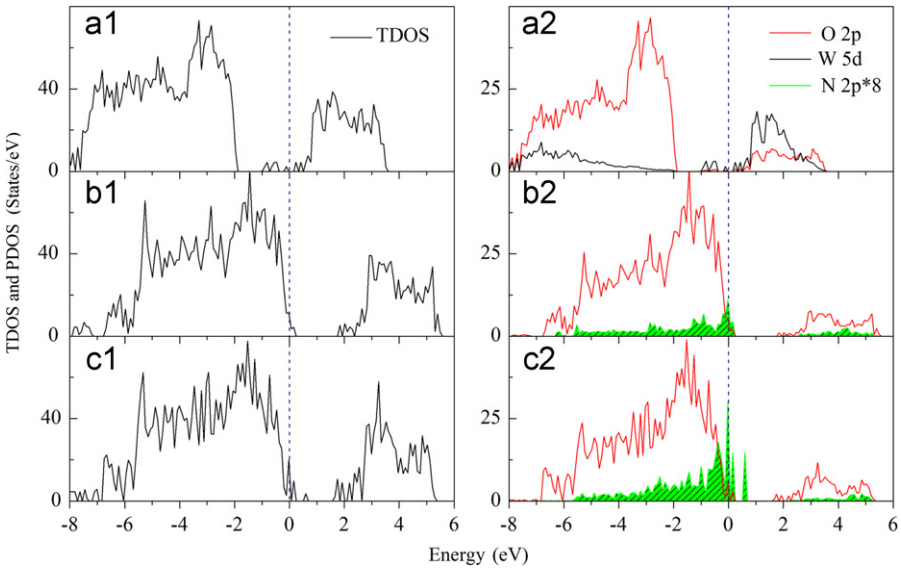

Fig. 5. The total and partial DOS of relaxed Bi_2WO_6: (a) with one O vacancy, (b) with one N atom, (c) with two N atoms. The navy dashed line represents the Fermi level. (For interpretation of the references to color in this figure legend, the reader is referred to the web version of this article.)

reduce the cation charge and coordination number leading to localized states in band gap and thus allowing excitation pathways to be initiated with sub-bandgap energy. [59–61] Comparing with that in pure cases, some W 5d and Mo 4d states depart from the CB emerging in the band gap of $Bi_{16}W_8O_{47}$ (Fig. 5(a2)) and $Bi_{16}Mo_8O_{47}$, respectively. The Fermi level shifts upward to the CB and locates in the band gap. These in-gap states near conduction band edge act as barrier of photogenerated electrons and form trapping center. This means that these in-gap states will hinder the electron transition from CB to VB and slow down the recombination of photoinduced carriers and then improve photocatalytic performance.

3.2.3. *N-doped Bi_2MO_6*

Fig. 3(d) shows that some new in-gap levels are introduced on the top of the VB in N doped Bi_2WO_6 ($Bi_{16}W_8NO_{47}$). The direct electron transition energy from these gap states to the CB is about 1.76 eV, which is reduced by 0.15 eV comparing with the pure Bi_2WO_6 and the decreasing trend is consistent with the experimental results reported by Shang et al. [31], and thus it confirms the redshift of N-doped Bi_2WO_6 observed in experiment. The TDOS and PDOS of N-doped Bi_2WO_6 shown in Figs. 5(b1) and (b2) indicate that the Fermi level falls into the VB, which means that each N atom requires one more electron from the lattice than does each O atom. The VB is predominantly composed of the hybridized states of O 2p and N 2p. Comparing with pure Bi_2WO_6, the substitution N for O results in the increases of the VB width by about 0.28 eV (6.67 eV vs. 6.95 eV) without the appearance of defect states in the band gap. This indicates that the increased mobility of photoexcited carriers in the VB and CB enhances the visible-light absorption and thus improves the photocatalytic behavior.

For Bi_2WO_6 doped with two N atoms ($Bi_{16}W_8N_2O_{46}$), more gap states near Fermi level are introduced and the intensity of DOS near the Fermi level is obviously enhanced compared with $Bi_{16}W_8N_1O_{47}$ (see Fig. 5(b2), (c2)). The band gap (1.65 eV) narrows by about 0.11 eV comparing with $Bi_{16}W_8N_1O_{47}$, which demonstrates that the electron transition energy decreases and the redshift of absorption edge of Bi_2WO_6 increases with the nitrogen doping concentration. This is in agreement with the previous experiment results reported by Shang et al. [31]. Consequently, higher nitrogen content in Bi_2WO_6 may enhance the visible light absorption and photocatalytic activity.

It is similar to $Bi_{16}W_8NO_{47}$, substitution N for O also introduces gap states near the top of the VB in Bi_2MoO_6 ($Bi_{16}Mo_8NO_{47}$), which results in the smaller electron direct transition energy from the gap states to the CB, 0.15 eV smaller than that of pure Bi_2MoO_6, and thus the redshift of adsorption edge occurs in N-doped Bi_2MoO_6. It is similar to Bi_2WO_6, for Bi_2MoO_6 doped with two N atoms ($Bi_{16}Mo_8N_2O_{46}$), the band gap of $Bi_{16}Mo_8N_2O_{46}$ decreases to 1.57 eV and the intensity of gap states increases with N concentration increasing. The electron transition energy decreases, which implies that the absorption edge of N-doped Bi_2MoO_6 may redshift with nitrogen doping concentration increasing.

The optical absorption spectra of pure Bi_2MO_6, N-doped Bi_2MO_6 and Bi_2MO_6 with oxygen vacancy were also calculated and shown in Fig. 6. To reduce the underestimation band gap for GGA method, the scissor operator corrections of 0.88 and 0.81 eV were applied in the absorption spectra for Bi_2WO_6 and Bi_2MoO_6, respectively. Fig. 6(a) shows that there is redshift of adsorption edges with nitrogen doping concentration increasing. The optical absorption curves of pure and N-doped Bi_2WO_6 are consistent with experimental optical absorption spectra [31]. At the same time, it directly shows that the O vacancy makes the aborption edge redshift and effectively improves the ability to absorb visible light. As to N-doped Bi_2MoO_6, the results are similar to Bi_2WO_6. Fig. 6 (b) shows that O vacancy and N dopants can result in redshift of adsorption edges. Meanwhile, along the increase of N-doping concerntration, the redshift will be more apparent. In addition, it directly shows that the O vacancy may effectively improve the ability to absorb visible light.

Usually, a higher doping level becomes relatively difficult in the experiment because a much larger formation energy is required, but there should be an optimal doping level [62]. Shang et al. pointed out experimentally the photoactivity of the sample is strongly dependent on the doping level and the atomic ration of N to Bi of 0.5 seems the best concentration for the photoactivity [31]. How to overcome the doping limitation to obtain higher dopant solubility in experiments and what is the best doping level for photoabsorption and photocatalytic effeciency are open issues.

Finally, we would like to refer to that the photocatalytic reactions consist mainly of three processes: (1) photoexcitation of electron and holes, (2) carrier transfers to the surface area, and (3) chemical reactions on the surface [57]. Our current study is related to the first two processes, which are determined by bulk

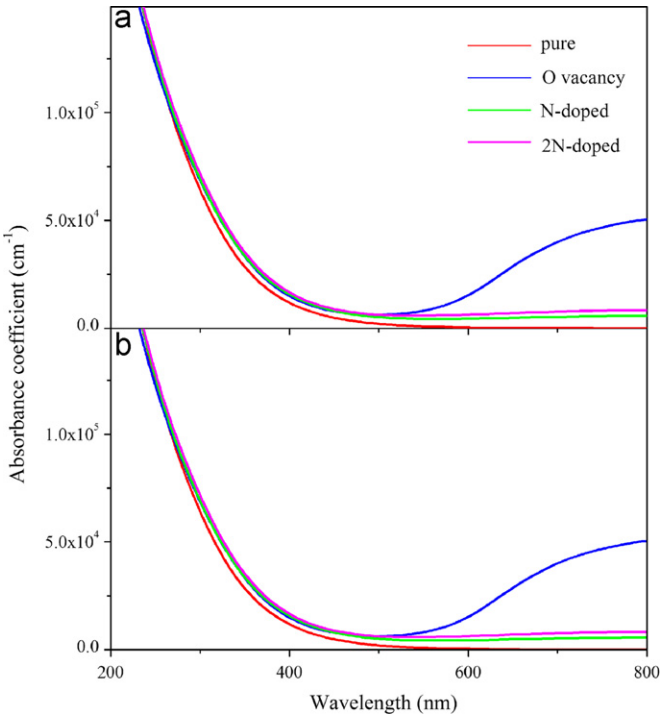

Fig. 6. The absorption spectra of pure Bi_2MO_6, Bi_2MO_6 with oxygen vacancy and N-doped Bi_2MO_6.

properties, such as electronic structures, and so on. Hence, there are some open issues. Whether the surface structure of Bi_2MO_6 is advantageous for the photocatalytic reactions? How to modify surface to improve reaction activity and efficiency? The answers to these issues are out of the scope of this work and are also left for future research.

4. Conclusion

The electronic structures of Bi_2MO_6 (M=Mo and W) with/without V_o and N-doping are studied by using first-principles calculations based on DFT within GGA scheme. The defects may induce localized geometry structural distortion and lead to the improvement of photocatalytic efficiency. The pure Bi_2WO_6 and Bi_2MoO_6 have similar band structures showing direct band gaps of 1.91 eV and 1.77 eV, respectively. The VBs are mainly composed of O 2p and Bi 6s, Bi 6p and a small part of M nd states, while the CBs are dominated by M nd, Bi 6p and a small part of O 2p states. The smaller effective mass in Bi_2WO_6 than in Bi_2MoO_6 may be responsible for the higher photocatalytic performance of Bi_2WO_6. V_O in Bi_2MO_6 (M=W, Mo) introduces localized W 5d or Mo 4d states in band gap, which may serve as a trapping center of photogenerated electrons and consequently improve photocatalytic reaction. Substitution of N for O induces hybrid states of O 2p and N 2p near the top of valence band, leading to the decrease of band gap and redshift of the photoadsorption. With increasing the nitrogen concentration, the band gap clearly decreases and the intensity of DOS near the Fermi level obviously becomes stronger.

Acknowledgments

This work is supported by the National Basic Research Program of China (973 program, Grant 2007CB613302), National Natural Science Foundation of China under Grant 20973102 and 11174180, Natural Science Foundation of Shandong Province under Grant ZR2011AM009, and Natural Science Foundation of Xinjiang Uygur Autonomous Region Department of Education under Grant XJEDU2011I52.

References

[1] A. Fujishima, K. Honda, Nature 238 (1972) 37.
[2] Z.G. Zou, J.H. Ye, K. Sayama, H. Arakawa, Nature 414 (2001) 625.
[3] A. Walsh, Y.F. Yan, M.M. Al-Jassim, S.-H. Wei, J. Phys. Chem. C 112 (2008) 12044.
[4] C.C. Wong, W. Chu, Environ. Sci. Technol. 37 (2003) 2310.
[5] A. Fujishima, T.N. Rao, D.A. Tryk, J. Photochem., Photobiol C1 (2000) 1.
[6] K.S. Yang, Y. Dai, B.B. Huang, M.-H. Whangbo, J. Phys. Chem. C 113 (2009) 2624.
[7] O. Carp, C.L. Huisman, A. Reller, Prog. Solid State Chem. 32 (2004) 33.
[8] K. Domen, A. Kudo, T. Onishi, J. Catal. 10 (1986) 217.
[9] J.W. Tang, Z.G. Zou, J.H. Ye, Angew. Chem. Int. Ed. 43 (2004) 4463.
[10] K. Sayama, H. Arakawa, J. Photochem. Photobiol., A 77 (1994) 243.
[11] Y. Inoue, T. Kubokawa, K. Stao, J. Chem. Soc., Chem. Commun. (1990) 1298.
[12] K. Sayama, H. Arakawa, J. Phys. Chem. 97 (1993) 531.
[13] D. Saha, S. Mahapatra, T.N. Guru Row, G. Madras, Ind. Eng. Chem. Res. 48 (2009) 7489.
[14] W. Wei, Y. Dai, B. Huang, J. Phys. Chem. C 113 (2009) 5658.
[15] J.B. Lu, Y. Dai, Y.T. Zhu, B.B. Huang, Chem. Cat. Chem. 3 (2011) 378.
[16] Y. Shimodaira, H. Kato, H. Kobayashi, A. Kudo, J. Phys. Chem. B 110 (2006) 17790.
[17] J.W. Tang, Z.G. Zou, J.H. Ye, Catal. Lett. 92 (2004) 53.
[18] A. Kudo, S. Hijii, Chem. Lett. 10 (1999) 1103.
[19] J.Q. Yu, A. Kudo, Chem. Lett. 34 (2005) 1528.
[20] H.B. Fu, C.S. Pan, W.Q. Yao, Y.F. Zhu, J. Phys. Chem. B 109 (2005) 22432.
[21] X. Zhao, T.G. Xu, W.Q. Yao, Y.F. Zhu, Appl. Surf. Sci. 255 (2009) 8036.
[22] L.H. Zhang, W.Z. Wang, Z.G. Chen, L. Zhou, H.L. Xu, W. Zhu, J. Mater. Chem. 17 (2007) 2526.
[23] H.B. Fu, L.W. Zhang, W.Q. Yao, Y.F. Zhu, Appl. Catal. B 66 (2006) 100.
[24] C.Y. Wang, H. Zhang, F. Li, L.Y. Zhu, Environ. Sci. Technol. 44 (2010) 6843.
[25] M. Shang, W.Z. Wang, S.M. Sun, L. Zhou, L. Zhang, J. Phys. Chem. C 112 (2008) 10407.
[26] L. Zhou, W.Z. Wang, L.S. Zhang, J. Mol. Catal. A: Chem. 268 (2007) 195.
[27] C. Belver, C. Adán, M. Fernández-García, Catal. Today 143 (2009) 274.
[28] H.H. Li, K.W. Li, H. Wang, Mater. Chem. Phys. 116 (2009) 134.
[29] H.B. Fu, S.C. Zhang, T.G. Xu, Y.F. Zhu, J.M. Chen, Environ. Sci. Technol. 42 (2008) 2085.
[30] R. Shi, G.L. Huang, J. Lin, Y.F. Zhu, J. Phys. Chem. C 113 (2009) 19633.
[31] M. Shang, W.Z. Wang, L. Zhang, H.L. Xu, Mater. Chem. Phys. 120 (2010) 155.
[32] J. Zhang, Z.H. Huang, Y. Xu, F.Y. Kang, Int. J. Photoenergy 2012 (2012), doi:10.1155/2012/469178.
[33] G. Kresse, J. Hafner, Phys. Rev. B 47 (1993) 558.
[34] G. Kresse, J. Furthmůller, Phys. Rev. B 54 (1996) 11169.
[35] P. Blöchl, Phys. Rev. B 50 (1994) 17953.
[36] J.P. Perdew, Y. Wang, Phys. Rev. B 45 (1992) 13244.
[37] J.P. Perdew, K. Burke, M. Ernzerhof, Phys. Rev. Lett. 77 (1996) 3865.
[38] H.J. Monkhorst, J.D. Pack, Phys. Rev. B 13 (1976) 5188.
[39] V.I. Anisimov, J. Zaanen, O.K. Andersen, Phys. Rev. B 44 (1991) 943.
[40] K.S. Knight, Mineral. Mag. 56 (1992) 399.
[41] R.G. Teller, J.F. Brazdil, R.K. Grasselli, J.D. Jorgensen, Acta Crystallogr. C40 (1984) 2001.
[42] M.S. Islam, S. Lazure, R. Vannier, G. Nowogrockib, G. Mairesse, J. Mater. Chem. 8 (1998) 655.
[43] J.-M. Herrmann, H. Tahiri, Y. Ait-Ichou, G. Lassaletta, A.R. Gonzales-Elipe, A. Fernandez, Appl. Catal., B 13 (1997) 219.
[44] I. Ilisz, A. Dombi, Appl. Catal., A 180 (1999) 35.
[45] G. Zhao, H. Kozuka, T. Yoko, Thin Solid Films 277 (1996) 147.
[46] G. Lassaletta, A.R. Gonzales-Elipe, A. Justo, A. Fernandez, F.J. Ager, M.A. Respaldiza, J.G. Soares, M.F. Da Silva, J. Mater. Sci. 31 (1996) 2325.
[47] H. Tada, K. Tiranishi, Y.-I. Inubushi, S. Ito, Langmuir 16 (2000) 3304.
[48] E. Stathatos, T. Petrova, P. Lianos, Langmuir 17 (2001) 5025.
[49] J. Sato, H. Kobayashi, Y. Inoue, J. Phys. Chem. B 107 (2003) 7970.
[50] Y. Yang, H. Zhong, C.X. Tian, Res. Chem. Intermed. 37 (2011) 91.
[51] Z. He, C. Sun, S.G. Yang, Y.C. Ding, H. He, Z.L. Wang, J. Hazard. Mater. 162 (2009) 1477–1486.
[52] X.F. Zhang, S. Chen, X. Quan, H.M. Zhao, Sep. Purif. Technol. 64 (2009) 309.
[53] Y. Hosogi, Y. Shimodaira, H. Kato, H. Kobayashi, A. Kuto, Chem. Mater. 20 (2008) 1299.
[54] W.T. Fu, Physica C 250 (1995) 67.
[55] L. Zhang, D.R. Chen, X.L. Jiao, J. Phys. Chem. B 110 (2006) 2668.
[56] H. Kato, A. Kudo, J. Phys. Chem. B 105 (2001) 4285.
[57] N. Umezawa, O. Shuxin, J.H. Ye, Phys. Rev. B 83 (2011) 035202.
[58] A. Janotti, D. Steiauf, C.G. Van de Walle, Phys. Rev. B 84 (2011) 201304.
[59] S.A. Bilmes, P. Mandelbaum, F. Alvarez, N.M. Victoria, J. Phys. Chem. B 104 (2000) 9851.
[60] Z.S. Lin, A. Orlov, R.M. Lambert, M.C. Payne, J. Phys. Chem. B 109 (2005) 20948.
[61] H.J. Zhang, G.H. Chen, D.W. Bahnemann, J. Mater. Chem. 19 (2009) 5089.
[62] K.S. Yang, Y. Dai, B.B. Huang, J. Phys. Chem. C 111 (2007) 12086.